PHILOSOPHICAL TRANSACTIONS A

rsta.royalsocietypublishing.org

Research

Article submitted to journal

Subject Areas:
solid mechanics, structural engineering

Keywords:
pure bending, buckling, thin shells, imperfection sensitivity, stability landscape

Author for correspondence:
Sergio Pellegrino
e-mail: sergiop@caltech.edu

Experimentally Probing the Stability of Thin-Shell Structures Under Pure Bending

Fabien Royer[1] and Sergio Pellegrino[2]

[1]Graduate Aerospace Laboratories, California Institute of Technology, 1200 E California Blvd, Pasadena CA 91125, USA
Currently at: Department of Aeronautics and Astronautics, Massachusetts Institute of Technology, Cambridge MA 02139-4307, USA
[2]Graduate Aerospace Laboratories, California Institute of Technology,1200 E California Blvd, Pasadena CA 91125, USA. ORCID 0000-0001-9373-3278

This paper studies the stability of space structures consisting of longitudinal, open-section thin-shells transversely connected by thin rods. subjected to a pure bending moment. Localization of deformation, which plays a paramount role in the non linear post-buckling regime of these structures and is extremely sensitive to imperfections, is investigated through probing experiments. As the structures are bent, a probe locally displaces the edge of the thin shells, creating local dimple imperfections. The range of moments for which the early buckling of the structures can be triggered by this perturbation is determined, as well as the energy barrier separating the pre-buckling and post-buckling states. The stability of the local buckling mode is then illustrated by a stability landscape, and probing is then extended to the entire structure to reveal alternate buckling modes disconnected from the structure's fundamental path. These results can be used to formulate efficient buckling criteria and pave the way to operating these structures close to their buckling limits, and even in their post-buckling regime, therefore significantly reducing their mass.

THE ROYAL SOCIETY PUBLISHING

1. Introduction

Thin shell structures are widely used in engineering applications. They enable lightweight structures of high stiffness and play a paramount role in the development of aerospace vehicles. As new applications are proposed and more advanced capabilities are sought, thinner shells are being designed and built. Recently progress in high-strain composites used in deployable space structures has accelerated this trend, with thin shell booms being used to support very large spacecraft structures [1,2].

However, one of the main challenges in using thin shell structures is the unpredictability of their buckling behavior. This complication lies in the physics of the buckling event. For thin shells, buckling is part of a family of instabilities called sub-critical bifurcations, which exhibit a rapidly falling post-buckling response in load/displacement space. If the post-buckling path does not regain stability, the structure loses its ability to carry loads. In many cases, the unstable post-buckling path is energetically close to the pre-buckling path (also called fundamental path), making the structure meta-stable near the bifurcation point. It is then possible for a small disturbance to transition the structure early into the post-buckling regime, overcoming the difference in total potential energy between the two states. The energetic proximity between the pre-buckling and post-buckling states also makes the structure extremely sensitive to imperfections, as first discovered in early experiments on cylindrical shells [3–5]. For a real structure, a small imperfection could easily erode the energy barrier between these two states, found in a theoretically perfect structure. The imperfection thus behaves like a connecting mechanism between these two states, causing the bifurcation point to be encountered earlier than theoretically predicted. This phenomenon becomes more pronounced as the thickness of the shell decreases.

In order to still be able to use these structures in practice, engineers try avoid buckling at all cost. For axially compressed cylindrical shells and pressurized spherical shells, numerous experiments were conducted and a lower bound on the statistical distribution of experimental buckling loads was determined. The difference between the theoretical buckling load and this empirical lower bound, called knockdown factor, has been the basis of practical cylindrical and spherical shell design for many years. It led to the NASA space vehicle design criteria for the buckling of thin-walled circular cylinders [6]. The classical knockdown factor design approach is powerful but has two major limitations. First, it is widely seen as very conservative, as it is based on the imperfections of shell structures built and tested many years ago, and therefore limits the potential mass savings of modern thin shells. Recent efforts by NASA's Shell Buckling Knockdown Factor (SBKF) Project have developed more realistic knockdown factors [7]. Second, each knockdown factor is only valid for a unique structure/loading combination and is therefore difficult to generalize to other kinds of structures and applications. It has been shown that knowing accurately a structure's initial geometry enables the accurate prediction of the buckling event [8,9]. However, in many applications, measuring the shape of a structure can be expensive and in some cases it is impossible.

In addition to imperfection sensitivity, localization of buckling deformations makes thin-shell buckling even harder to predict. It causes significant differences between theoretical buckling eigenmodes and experimentally observed deformed shapes. Localization arises in two situations. The first corresponds to post-buckling localization and is a manifestation of the extremely non-linear response of the structure beyond the bifurcation. In this case, the onset of the buckling eigenmode appears at the exact point of bifurcation, and greatly affects the structure's geometric stiffness. As the loading is increased, the deformation of the structure concentrates at specific locations, given by the peak eigenmode amplitude and/or by dominant imperfections. In this case, the buckling mode initially triggers a global, but very small deformation that gradually becomes more and more localized. This type of localization is for instance observed in beams on an elastic foundation [10] and in spherical shells under external pressure [11–13]. Another localization scenario is observed when a global post-buckling mode is created through the sequential formation of localized buckles. It features a series of destabilizations and restabilizations of the post-buckling path, known as snaking [14]. Interestingly, the first localized buckle can appear on post-buckling paths disconnected from the fundamental path, while running asymptotically close to it [15]. This phenomenon is observed in cylindrical shells for which a single dimple, "broken away" from the unbuckled state, evolves into a fully periodic buckling mode through snaking [15,16]. It has been shown that for the cylindrical shell, the single-dimple state sits on a mountain pass in the energy landscape, between the pre-buckling and post-buckling states, and is the lowest critical escape mechanism by which the structure can buckle [17]. Since the location at which deformations localize depends heavily on the imperfections present in the structure, a large number of different post-buckling solutions can be generated by a small set of theoretical eigenmodes. This situation is referred to as spatial chaos [18].

The imperfection sensitivity driving the buckling behavior is then twofold. It erodes the energy barrier between pre-buckling and post-buckling states, causing early buckling, and it also creates a high number of possible post-buckling paths, through localization. For these reasons, predicting buckling is extremely difficult for shell structures and often relies on a case by case approach. Recent work has focused on the sensitivity of the buckling phenomenon to disturbances in thin cylindrical and spherical shells. A non-destructive experimental method to study the meta-stability of the unbuckled state has been proposed. It focuses on determining the energy barrier separating the fundamental path from the critical localized post-buckling state [19–21]. The search for the load at which the critical buckling mechanism can be triggered is carried out by imposing a local radial displacement in the middle of the structure using a probe. This method effectively quantifies the resistance of shell buckling against the single dimple imperfection mentioned earlier. The method has been successfully applied to cylindrical shells [22] and pressurized hemispherical shells [23]. These experiments quantified in particular the onset of meta-stability, often referred to as "shock sensitivity" [24], and a comparison with historical test data has shown that this specific loading can provide an accurate lower bound to experimentally observed buckling loads [15,25], thus leading to more realistic knockdown factors. A similar probing methodology has also been applied to circular arches [26], cylindrical shell roofs [27], and prestressed stayed columns [28], and the use of multiple probes has enabled the exploration of the complete unstable behavior of these structures, beyond limit and branching points.

This paper extends the experimental probing methodology, previously used for cylindrical and spherical shells, to more complex structures that are inspired by ultralight coilable space structures, recently developed by the Caltech Space Solar Power Project (SSPP) [29,30]. Previous analysis showed that local buckling plays a key role in these structures [31,32] and motivates the need for an experimental buckling characterization. Due to the complexity of an actual SSPP structural component, as well as reproducing its actual load conditions, the present study focuses on the simpler structure studied analytically in [33] and loaded under pure bending. Similarly to the space application, the structure in the present study is composed of two open cross-section thin-shell components connected by transverse rods. While the structure and loading are different, the problem studied in the present paper is more general and its conclusions are more broadly representative of the buckling of structures featuring thin-shell open cross-sections.

An important characteristic of the structure studied in this paper is that its post-buckling path restabilizes and, therefore, the maximum moment that can be carried by the structure is greater than the first buckling moment [31,32]. This behavior offers a unique opportunity to study the behavior closer to the buckling event than ever before. In fact, it has been suggested that the SSPP structures could be allowed to operate in the post-buckling regime.

To achieve these goals, the present paper shows that by using the experimental probing methodology, the meta-stable behavior of the structure close to buckling can be fully characterized. This knowledge can be used to derive efficient buckling criteria based on disturbance levels, or the minimum load at which meta-stability arises. The methodology can then be extended to navigate spatial chaos in the post-buckling regime, where competing paths can be identified and a range of possible post-buckling responses determined. The overall philosophy is embracing buckling rather than avoiding it, in order enable the design of much lighter structures.

The paper is structured as follows. Section 2 describes the test structure and a novel experimental setup to carry out probing tests under bending. Following a classical buckling analysis, Section 3 highlights the importance of localization and spatial chaos by comparing finite element simulations with the experimental buckling response. In Section 4, probing experiments study the formation of the buckling mode and characterize its meta-stable behavior. In Section 5, probing along the entire structure determines alternate locations at which local buckling can appear, and the formation of alternate buckling modes is studied through additional probing. The consequences of the appearance of these alternate modes on the global bending response are then highlighted, and Section 6 concludes the paper.

2. Test structure and experimental setup

The test structure, referred to as a strip, consists of thin-shell longerons (tape springs [34]) connected by transverse battens. It is shown in Figure 1. The longerons were made from Craftsman 1-in stainless steel tape measure, which has similar size and thickness to the cross-section used in structures for space applications but is much more readily available available. The thickness is $t = 110\ \mu$m and the length $L = 714$ mm, plus 6 mm on each end for embedment in the end plates. The longeron cross-section is a circular arc with 14 mm radius and 75 deg subtended angle, with 3 mm straight extensions on the extremities, Figure 1b. The battens were cut from a pultruded carbon fiber rod of diameter $d = 2$ mm, to lengths $l = 50$ mm of which 3 mm were embedded in the rivets on each end. The measured Young's modulus of the longerons is $E_1 = 208$ GPa and the Poisson's ratio $\nu = 0.3$. The battens Young's modulus is $E = 140$ GPa.

To build a strip, four battens were inserted into metal rivets placed into tight-fitting holes at a spacing of 145 mm in the longerons. Blobs of epoxy were used to achieve a full connection between the longerons and the battens. The ends of the longerons were inserted and glued into 6 mm thick acrylic plates with 0.2 mm wide laser cuts following the shape of the longeron cross-section. The acrylic plates serve as the interface between the structure and the bending machine.

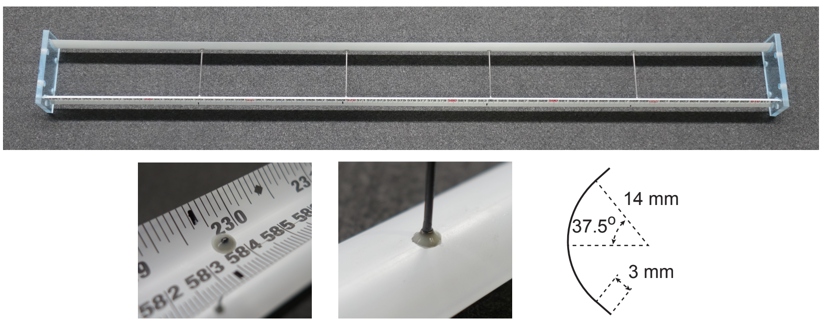

(b) (c) (d)

Figure 1: (a) Test structure with stainless steel longerons connected by carbon fiber rods. (b) Front and (c) back connection between batten, rivet, and longeron. (d) Longeron cross-section.

The bending machine is shown schematically in Figure 2. The machine employs two perpendicular linear guides with air bearings that both translate and rotate, to guarantee that no parasitic reaction forces can arise. Only a pure bending moment is applied to the test structure. A detailed description is available in Ref. [35].

There are two slider assemblies, consisting of several components mounted on identical air bearings. The actuated slider, on the left, consists of a DC motor (Harmonic Drive FHA-8C)

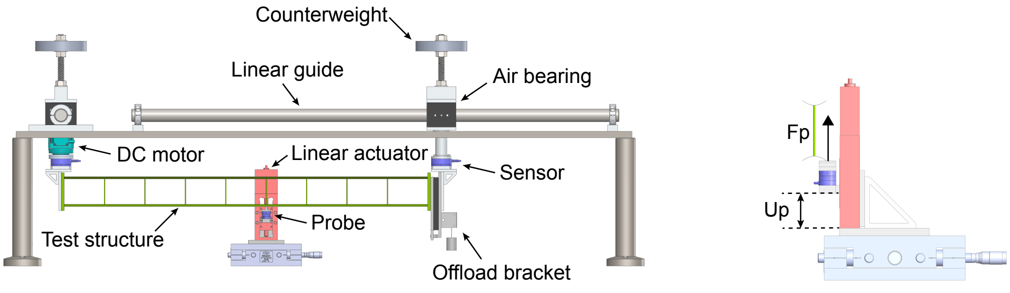

(a) (b)

Figure 2: (a) Bending machine and probing stage. (b) Probing details, U_p, F_p are vertical.

which rotates the test structure around the axis of the slider assembly. The rotation profile follows a smooth s-curve with maximum angular velocity set to 0.05 deg/s to limit dynamic effects. An incremental encoder with a resolution of up to $800,000$ counts per revolution measures the applied rotation (around the axis of the slider assembly). A force/torque sensor (ATI Mini40) is attached to the motor's rotating end and can measure bending moments up to 2 Nm. An aluminum bracket is mounted on the sensor and provides an interface to attach the test structure. The passive slider, on the right, has an aluminum tube instead of the DC motor. An offload bracket allows the right-hand side of the structure to translate along the axis of the slider assembly. It uses a hanging mass and pulley to compensate for half of the mass of the test structure and half of the mass of the bracket's translating assembly. Note that the axes of the slider assemblies are vertical at the beginning of each test, but then rotate by small angles during the test.

To avoid parasitic moments caused by gravity, a counterweight is mounted on top of each slider assembly and its height is adjusted to balance the assembly around the axis of the air bearing. Note that, although only the moment at one end of the test structure needs to be measured, sensors are mounted on both ends. The average of the two end bending moments is the value reported in this paper.

The test structure is perturbed by a "probe" that locally displaces a longeron. The probing apparatus is composed of a motorized linear stage (Newport MFA-CC) providing a positioning accuracy of ± 3 μm. A force sensor (ATI Nano17) is mounted on the moving part of the stage and supports a Teflon wedge that comes into contact with the longeron edge when probing is applied. The sensor measures the probe force with a resolution of $1/320$ N, and an incremental encoder on the motorized stage measures the probe displacement with a resolution of 0.0177 μm.

When the structure is bent into an arc, the inner side of the arc is under compression and the outer side is under tension. The maximum compressive stress occurs on the inner edges of both longerons. The probe wedge axis is perpendicular to the longeron edge and there is a point contact between the longeron and the wedge. As the longeron is probed by moving the wedge vertically up, the longeron cross-section flattens.

3. Classical buckling analysis and experiment

(a) Buckling eigenmodes

The first step in understanding how buckling unfolds is to conduct a buckling eigenvalue analysis, with the goal of detecting the bifurcations that exist on the structure's pre-buckling path (fundamental path). This analysis gives insights into the buckling loads/rotations and also unveils the additional buckling modes that can be found above the first bifurcation. Knowing the buckling modes is important, since the buckling modes and the imperfections with the greatest influence on buckling are related. The buckling modes also identify the deformed shapes to be expected once the structure has buckled.

A finite element model was set up in Abaqus 2018, to replicate the structure's geometry, materials, and the bending machine's boundary conditions. Computation of the "exact" buckling eigenmodes and moments, requires an iterative procedure, because the fundamental path of thin shell structures can exhibit significant geometric nonlinearity [36]. The first iteration follows a classical buckling analysis. A linear perturbation is applied to the stress-free structure and buckling moment estimates are computed. The strip is then loaded by a bending moment, under the first buckling moment estimate, and the problem is linearized about this new pre-stressed state, taking into account pre-buckling nonlinearities. This process is repeated until the first buckling moment estimate converges to its "real" value.

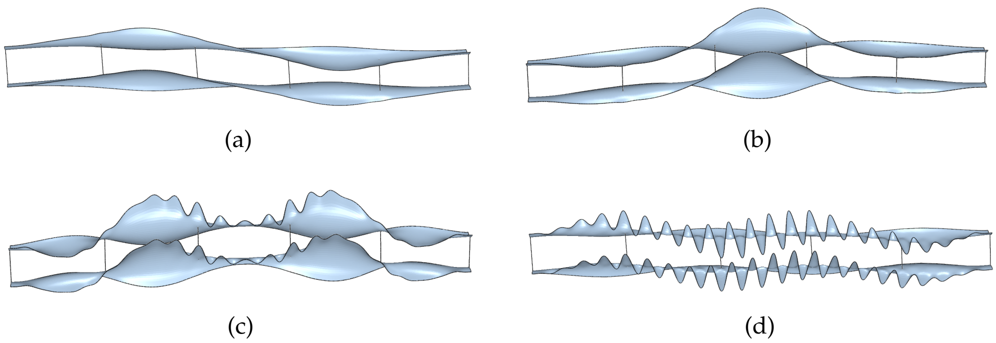

Figure 3: Buckling eigenmodes determined through finite element simulations. (a) First ($M_{cr} = 1.604$ Nm), (b) second ($M_{cr} = 1.759$ Nm), (c) third ($M_{cr} = 2.003$ Nm), and (d) fourth ($M_{cr} = 2.009$ Nm) eigenmodes.

The above analysis yielded four bifurcation points, and the corresponding buckling eigenmodes are shown in Figure 3. The first two eigenmodes are dominated by long wavelength deformations spanning the entire length of the longerons, and therefore can be described as global modes. The last two eigenmodes feature short wavelength deformations modulated in amplitude by a long wavelength deformation. Note that, in Figure 3, the amplitude of these deformations is arbitrary since the eigenmodes have been normalized. From this analysis, a first buckling moment of approximately $M_{cr} = 1.6$ Nm (corresponding to a rotation of 2.1 deg) would be expected, as well as a post-buckling deformed shape resembling the first eigenmode, Figure 3a.

However, the classical buckling eigenvalue analysis has two main limitations. First, it does not take into account the imperfections of the real structure, which can change the order of the bifurcations, and prioritize one buckling eigenmode over another. The post-buckling deformed shape often results from a linear combination of the first few buckling modes, if the corresponding buckling moments are relatively close. Second, thin shells exhibit buckling mode localization, as explained in Section 1. In most cases, even for a perfect structure, the computed eigenmode is only valid at the bifurcation point, and deformations localize at one or more preferred locations as soon as the structure transitions to its post-buckling regime.

(b) Moment/rotation response and post-buckling localization

A set of five bending experiments were carried out, with a maximum rotation $\theta_{max} = 3$ deg . The mean and standard deviation of the moment/rotation responses are shown in Figure 4a.

The figure shows that the response is linear until the structure bifurcates for $\theta_{cr} = 1.74$ deg and $M_{cr} = 1.25$ Nm. The structure undergoes a snap-back and restabilizes at $M_{cr} = 1.09$ Nm. Note that the experimental buckling moment is 22% lower than the first theoretical bifurcation, which highlights the imperfection sensitivity of the structure. In the experiment, the snap-back occurs over a small range of rotations, and a quasi-static response (vertical tangent) would be observed for a lower rotation rate. The post-buckling regime is stable for both moment and rotation-controlled cases, and the response is weakly non-linear. In further tests, presented in

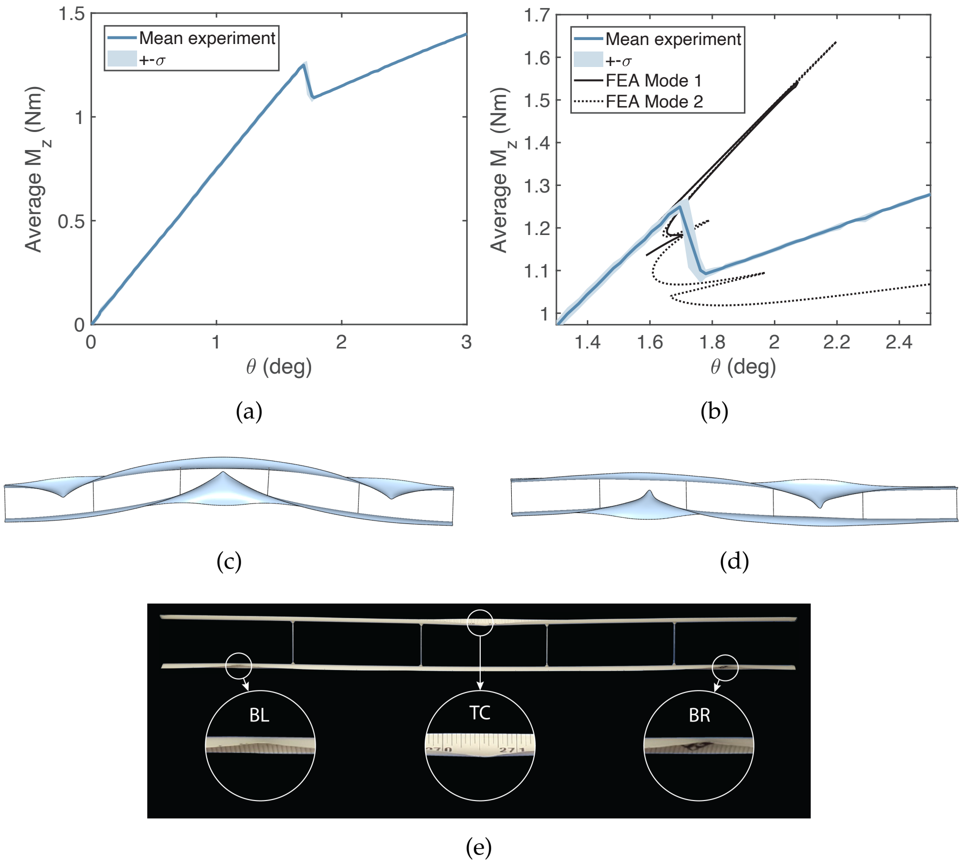

Figure 4: (a) Mean experimental moment/rotation curve and standard deviation for five bending experiments. (b) Comparison between experiment and FEA near bifurcation point. Post-buckling modes obtained by FEA when seeding imperfections based on (c) second and (d) first buckling eigenmodes. (e) Experimental post-buckling shape.

Section 5(d), the maximum rotation was extended to $\theta_{max} = 10$ deg to confirm that the stable post-buckling regime extends to larger bending moments.

To compare the experimental response with finite element simulations, the post-buckling paths corresponding to the first two eigenmodes were computed with a standard method [37,38]. Each mode was seeded in the structure's initial geometry as a geometric imperfection with amplitude set to 30% of the shell thickness. The modified Riks solver available in Abaqus was used to trace the stable and unstable part of the post-buckling response. These paths are shown in Figure 4b together with the experimental response. The corresponding deformed shapes at the end of the two post-buckling paths are shown in Figure 4c (second mode) and 4d (first mode).

In both cases, the post-buckling shapes exhibit significant differences with the buckling eigenmodes. They feature highly localized deformations extending inward (towards the structure's longitudinal axis) and forming a series of alternating buckles. The buckle locations coincide with the inward peak deformations found in the eigenmode. It is noticed that here the localization phenomenon prioritizes inward deformations, as no outward buckles are found. The post-buckling paths feature a snaking sequence, characterized by a series of destabilization and restabilization events. Snaking physically corresponds to the sequential formation of buckles. For the post-buckling path corresponding to the second mode, the structure bifurcates at higher moments than for the first mode, as expected from the eigenvalue analysis. The central buckle formation corresponds to the first post-buckling fold, directly connected to the unbuckled path, while the side buckles form in the second and third folds.

The post-buckling shape corresponding to the first mode forms in a similar way. The structure bifurcates around $M = 1.58$ Nm and the first fold corresponds to the formation of one of the two buckles. When the second destabilization point (called snaking point) is reached, the second buckle starts to form. However, the simulation is stopped before the path restabilizes, as the two buckles compete, causing the solver to oscillate between forming one buckle or the other. Continuing the simulation was not attempted here, but it would be possible, e.g., by tweaking the initial imperfection.

Next, the simulation results and the experiment are compared. The deformed shape obtained experimentally, after applying a rotation of $\theta = 3$ deg, is shown in Figure 4e. It matches exactly the post-buckling shape found in simulation for the second eigenmode imperfection even if, in theory, the lowest bifurcation corresponds to the first eigenmode. Note that top and bottom longerons are interchangeable in Figure 4c-d since no gravity is applied in the simulation. In addition, significant differences exist between the two post-buckling paths. The experimental post-buckling restabilizes at a higher moment, and the post-buckling stiffness is also higher.

This result highlights the limitations of a purely simulation-based design and analysis approach for the structures studied in this paper. In particular, the transition to buckling happens at a significantly lower moment, due to the structure's imperfection sensitivity. Only two types of geometric imperfections are considered here, but any linear combinations of the four eigenmodes would potentially yield a different post-buckling solution corresponding to a different localization mechanism, which is a characteristic of spatial chaos [39].

Note that it would be possible to find all of the potential post-buckling paths for the perfect structure using an advanced computational method, such as path-following [40]. However these methods are not usually available in commercial finite element software, and can only be matched with experiments if the real imperfections in the structure are known. Indeed, in reality, various post-buckling modes compete and the structure's imperfections determine which path connects to the unbuckled state. This path does not necessarily coincide with the solution given by the lowest eigenmode, and many paths can run close to the unbuckled path without ever intersecting it. These alternate modes can be accessed if a small perturbation is applied to the structure, causing early buckling. This meta-stable behavior is explored in the next section, using probing experiments.

4. Probing the experimentally observed post-buckling mode

This section focuses on the formation of the post-buckling mode that is obtained without applying any perturbations to the structure. This specific mode is referred to as the main post-buckling mode.

When a rotation of $\theta_{cr} = 1.74$ deg was imposed, the bifurcation point was reached and the structure experienced a snap-back, during which three buckles formed simultaneously. They are shown in Figure 4e, and are referred to as the Top-edge Central (TC) buckle, the Bottom-edge Right (BR) buckle, and the Bottom-edge Left (BL) buckle.

In reality, the formation of these buckles follows a specific snaking sequence, resembling the simulated post-buckling paths of Figure 4b. However, in a rotation-controlled experiment, unstable portions of the response are not captured, and hence the snaking sequence is hidden by the snap-back event. The formation of the first local buckle triggers the formation of the second buckle and subsequently of the third one. These buckles interact with each other through global structural deformations (torsion, in-plane and out-of-plane bending). However, close to the buckling load, the structure is meta-stable and equilibrium configurations featuring one or more of these local buckles can be attained if a small perturbation is applied to the structure. Of particular interest is the lowest rotation/bending moment at which these buckles can be found in equilibrium, and the energy barrier that needs to be overcome to form them.

The three buckle locations (TC, BR and BL) were individually probed. For a fixed rotation, the longeron's edge in compression was locally displaced at each of the three buckle locations, and the probe reaction force was measured. The rotation increment was initially set to 0.05 deg and

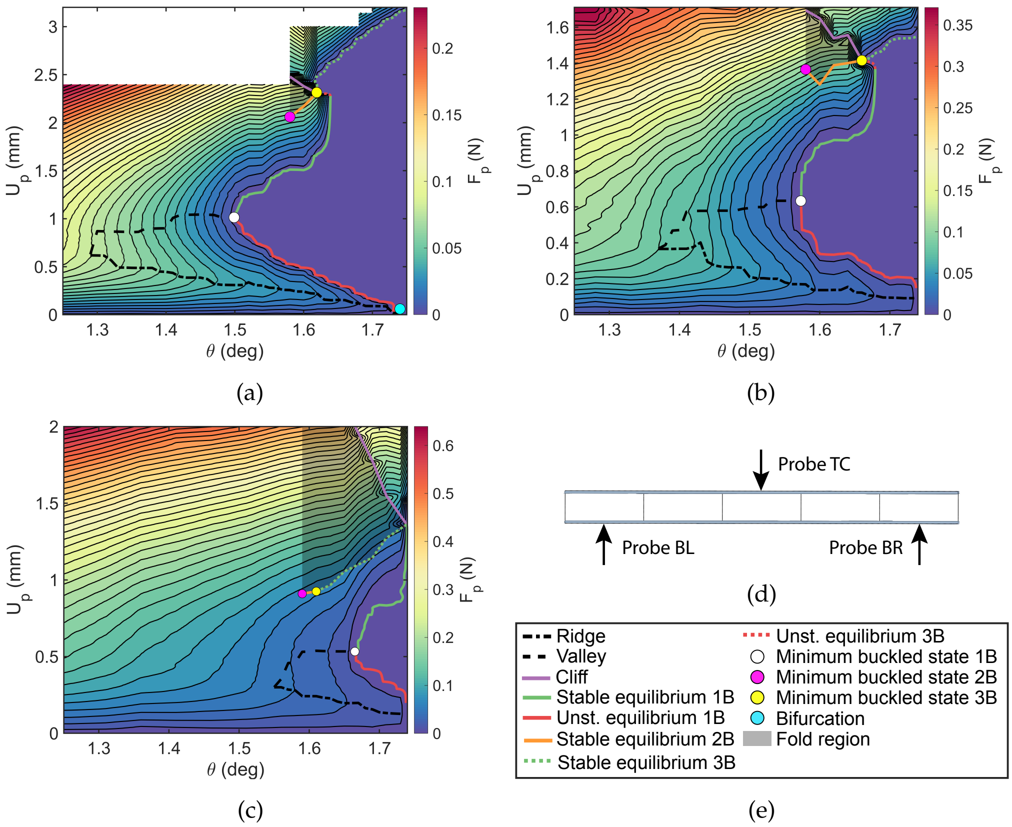

Figure 5: Stability landscapes for (a) TC, (b) BR, and (c) BL probe location. (d) Schematic of strip structure with three probe locations. (e) Legend.

refined to 0.02 deg when probing near the ridge and valley. Note that the chosen probing scheme is compatible with the kinematics of the buckle formation, and hence does not affect the natural deformation of the structure.

The three stability landscapes obtained from these tests, which display the probe force as a function of the rotation and the probe displacement, are shown in Figure 5. They give insights into which combinations of buckles can be observed before the bifurcation point and identify the critical buckle responsible for the transition into the post-buckling regime. This representation was first introduced in 2016 [22] for cylindrical shells and here has been extended to more complex structures.

(a) Top-edge central probing (TC)

The top-edge central buckle location (TC) was probed first and the results of this experiment are shown in Figure 5a.

For $\theta < 1.29$ deg, the probe force F_p increases monotonically as the probe displacement U_p is increased, and the probe force is close to linear with respect to the probe displacement when the applied rotation is small ($\theta < 0.5$ deg). When the rotation is increased, the probe force versus probe displacement characteristic is no longer monotonic, and a region of negative probe stiffness appears, resulting in two important features of the stability landscape. The local maximum of probe force forms the ridge (dashed and dotted line) and the local minimum forms the valley (dashed line). In a force-controlled probing experiment, the structure would undergo a snap-through instability and kinetic energy would be released. For probe displacements larger than the critical valley displacement, the probe force increases monotonically again.

As the rotation is increased, the probe force in the valley decreases until reaching $F_p = 0$ N for $\theta = 1.5$ deg. This point corresponds to the smallest value of the rotation at which a single local buckle (labeled 1B) can be formed and can remain in equilibrium at the probe location. This value is referred to as the single-buckle minimal buckling rotation and corresponds to the minimally buckled state found at the end of the valley. Tracing the ridge, the displacement decreases as the rotation increases until the ridge disappears at the point of spontaneous buckling (bifurcation point), for $\theta_{cr} = 1.74$ deg. The stable (solid green) and unstable (solid red) single-buckle equilibrium contours, for which $F_p = 0$ N, originate from the single-buckle minimally buckled state. Above the minimal buckling rotation, the structure undergoes a snap-through instability when the probe displacement reaches the unstable equilibrium contour. At this point, the probe loses contact with the longeron and $F_p = 0$ N. Contact is restored when the probe displacement reaches the stable equilibrium contour. The region in which there is no contact between the probe and the longeron is referred to as the lake. If the probe were able to apply tension in addition to compression, the landscape would feature negative probe forces in the lake.

Probing has revealed three types of equilibria, accessible if a disturbance provides enough energy to the structure. The energy barrier separating the unbuckled and buckled states can be computed by integrating the probe force as a function of the probe displacement. An analysis of the energy barrier is presented in Section 4.d. For $U_p < 2.3$ mm and $\theta < 1.64$ deg, the single buckle equilibria (labeled 1B) are found. However, for $1.58 < \theta < 1.62$ deg, the probed structure undergoes instabilities (fold region in Figure 5a) past the stable single dimple equilibrium contour. A probe characteristic featuring this instability is shown in Figure 6 for $\theta = 1.6$ deg. This type of instability is called a cusp catastrophe [41].

When the probe reaches the cliff (in purple in Figure 5), the structure undergoes a snap-back and the probe force drops. Hence, the cliff corresponds to limit points at which the tangent to the probe characteristic is vertical. At this point, the probing path becomes unstable, folds, and eventually restabilizes at lower values of the probe force. In the displacement-controlled probing experiment, the unstable portion of the path cannot be captured and the structure directly snaps to the lower (and stable) part of the fold.

When retracted, the probe follows the entire stable probe characteristic until the probe force reaches $F_p = 0$ N. The equilibrium contour for the two stable buckles (2B), shown in orange in Figure 5 and marked on Figure 6a, is then found. On this contour, buckles appear at the TC and BR locations. Note that the structure would naturally evolve to the two-buckle stable contour if the probe is removed after the cliff. If the probe displacement is further decreased, the probe loses contact with the longeron and the two buckles remain in equilibrium. Because kinetic energy is released during the snap-back event for the unstable probing characteristic, and during the snap-through even for the "well behaved" probing characteristic, the energy barrier to return to the undeformed configuration may be different from the buckling energy barrier. A comparison of these two quantities could be the subject of future work. The shaded region represents the top view of the fold (or cusp). The smallest rotation at which the two buckles equilibria are found is $\theta = 1.58$ deg and is referred to as the two buckles minimal buckling rotation.

Finally, returning to Figure 5 for $\theta > 1.62$ deg, equilibria featuring the full buckling pattern (3 buckles) are found. For a fixed rotation within the range $1.62 < \theta < 1.64$ deg, the TC buckle is created first. However, as the probe displacement is increased past the unstable three buckles (3B) equilibrium contour (dotted red), the structure experiences a snap-through and the probe loses contact with the longeron until it reaches the stable three buckles equilibrium contour (dotted green). For $\theta > 1.64$ deg, any probing past the single-buckle equilibrium contour results in a direct snap-through to the three buckles equilibrium contour. If the stable single buckle is formed, and the rotation is increased without any probing, the structure will follow the single-buckle equilibrium contour until $\theta = 1.64$ deg, for which the three buckles pattern forms. This rotation is referred to as the snaking rotation. This observation reveals that the snaking sequence

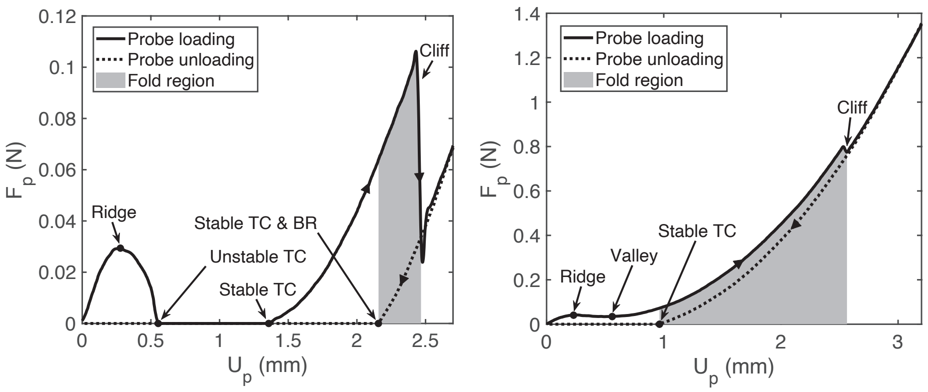

(a) (b)

Figure 6: Loading and unloading probe force/displacement characteristic, for $\theta = 1.6$ deg, at (a) TC and (b) BL probe location. The BR response closely resembles (a).

is only composed of two folds corresponding to the buckling of the top longeron, followed by the buckling of the bottom longeron, even if the buckling pattern features three buckles.

(b) Bottom-edge right probing (BR)

The structure was unloaded and the probing experiment was repeated for the bottom edge right buckle location (BR). The results are shown in Figure 5b, which is discussed next.

The BR stability landscape exhibits the same features as the TC landscape. At $\theta = 1.37$ deg, the ridge and valley start. The valley ends at the single-buckle minimum buckling state, $\theta = 1.56$ deg, which is the point where the unstable and the stable single-buckle, at location BR, equilibrium contours start. At the point of spontaneous buckling, corresponding to $\theta_{cr} = 1.74$ deg, the BR and TC probing behaviors are different. For the BR location, the ridge does not intercept the unbuckled state ($U_p = 0$ mm) and ends abruptly. The unstable single buckle contour is therefore offset from the unbuckled state. Such a buckling mode is often referred to as a broken away mode [15].

This important observation suggests that while the TC buckle can be formed at the bifurcation point, the BR buckle can only appear later in the snaking sequence, for the unperturbed structure. When perturbations are applied, the BR buckle can be triggered earlier, if the energy barrier separating the unbuckled state and the unstable single-buckle state is overcome. For $1.58 < \theta < 1.66$ deg, a two-buckle pattern can be formed in the unstable probing region (fold region). Similarly to the TC probing, once the probe displacement exceeds the cliff, the probe characteristic follows a different path when retracted, and the two buckles equilibrium contour features the TC buckle in equilibrium with the BR buckle. Finally the three buckles pattern can be formed through large amplitude probing, for $1.66 < \theta < 1.68$ deg. Above the snaking rotation, for $\theta = 1.68$ deg, the structure experiences a snap-through to the stable three-buckle contour as soon as the probe displacement exceeds the unstable single-buckle contour.

(c) Bottom-edge left probing (BL)

Lastly, the probing experiment was repeated for the bottom edge left buckle location (BL), and the results are shown in Figure 5c.

For this probing location, the ridge and valley appear at $\theta = 1.55$ deg, later than for the BR and TC probing. The single buckle minimal buckling rotation is found at $\theta = 1.67$ deg, i.e., close to the point of spontaneous buckling. Similar to the BR probing, the stability landscape appears truncated at the bifurcation rotation, and the unstable single-buckle equilibrium contour is disconnected from the unbuckled state. This feature suggests that, similarly to the BR buckle, the BL buckle can only be formed through snaking or a perturbation. The difference in behavior between BR and BL probing is most likely caused by local imperfections at the probe locations, and at the strip supports.

For $1.59 < \theta < 1.74$ deg, the stability landscape features a cliff beyond which the probe snaps-back. Similarly to the TC and BR probing locations, once the cliff displacement is exceeded, equilibria are found when the probe retracts. For $1.59 < \theta < 1.61$ deg, the TC buckle is in equilibrium, without the BL buckle being present. The TC buckle quickly evolves to the fully formed buckling pattern above the three-buckle minimum buckling rotation, $\theta = 1.61$ deg. Note that the-three buckle equilibria can be obtained at rotations lower than the BL buckle minimum buckling rotation. Contrary to the two previous probing locations, once the stable single BL buckle is formed and the structure follows its stable equilibrium contour, the fully formed buckling pattern will not appear prior to reaching the point of spontaneous buckling.

(d) Energy barriers and early formation of buckling patterns

The stability landscapes have shown that the three buckles belonging to the main post-buckling mode can appear in the structure before the bifurcation point is reached. These equilibria are attained if a perturbation that provides enough energy to overcome a critical threshold is applied to the structure. The energy barriers for the three probing locations (TC, BR and BL) were computed for all of the buckle combinations identified in the previous subsection.

In Figure 7a, the solid line corresponds to the energy needed to go past the unstable TC contour and snap to the stable TC equilibrium. The dashed line is obtained by adding the energy required to reach the cliff. The dotted line for $1.62 < \theta < 1.64$ deg is obtained by adding the energy needed to reach the unstable TC, BR and BL contour. Finally, for $\theta > 1.64$ deg, the dotted line corresponds to the energy needed to reach the unstable TC contour, after which the structure snaps to the stable TC, BR and BL contour. Figures 7b and 7c are constructed in a similar way.

For a fixed rotation, the work done by the probe is found by integrating the probe force as a function of the probe displacement. The energy barrier to form a specific combination of dimples corresponds to the maximum value of the probe work between the unbuckled state ($U_p = 0$ N) and the corresponding buckled equilibrium. The energy barriers for the three probing locations are shown in Figure 7.

Focusing first on the energy barriers for the TC probing location, Figure 7a shows that for $1.5 < \theta < 1.64$ deg, forming the TC buckle requires the smallest amount of energy. However if more energy is provided to the structure, the TC and BR buckle configuration can be obtained, which transitions to the full buckling pattern above the three buckles minimum buckling rotation of $\theta = 1.62$ deg. Above the snaking rotation of $\theta = 1.64$ deg, probing past the unstable TC equilibrium always results in the three buckles pattern formation. The energy barrier decreases continuously until reaching 0 mJ at the bifurcation point, confirming that the TC buckle appears first in the snaking sequence.

A similar energy barrier distribution is observed for the BR probing location, as shown in Figure 7b. The lowest energy barrier branch corresponds to the single BR buckle formation which transitions to the full buckling pattern above the snaking rotation of $\theta = 1.68$ deg. The highest energy barrier branch corresponds to the same buckle combinations found for the TC probing location. The TC and BR buckle disappear to form the full buckling pattern for $\theta = 1.66$ deg.

In theory, this rotation should coincide with the three buckles minimal buckling rotation found for the TC probing. In practice, the relative difference between the two rotations is less than 2%, and this small discrepancy can be due to small variations in the structure's initial configuration for the two probing experiments. It should also be noted that the small amplitude of the BL buckle makes its detection difficult. When the rotation increases, the three buckles energy barrier decreases slowly and plateaus without reaching the 0 mJ threshold. This result confirms that the BR buckle cannot be formed through a fundamental path bifurcation, and hence is indeed a broken-away mode.

Finally, the energy barriers for BL probing are shown in Figure 7c. Two energy barrier branches are found. The lowest energy barrier branch starts at the single buckle minimum buckling

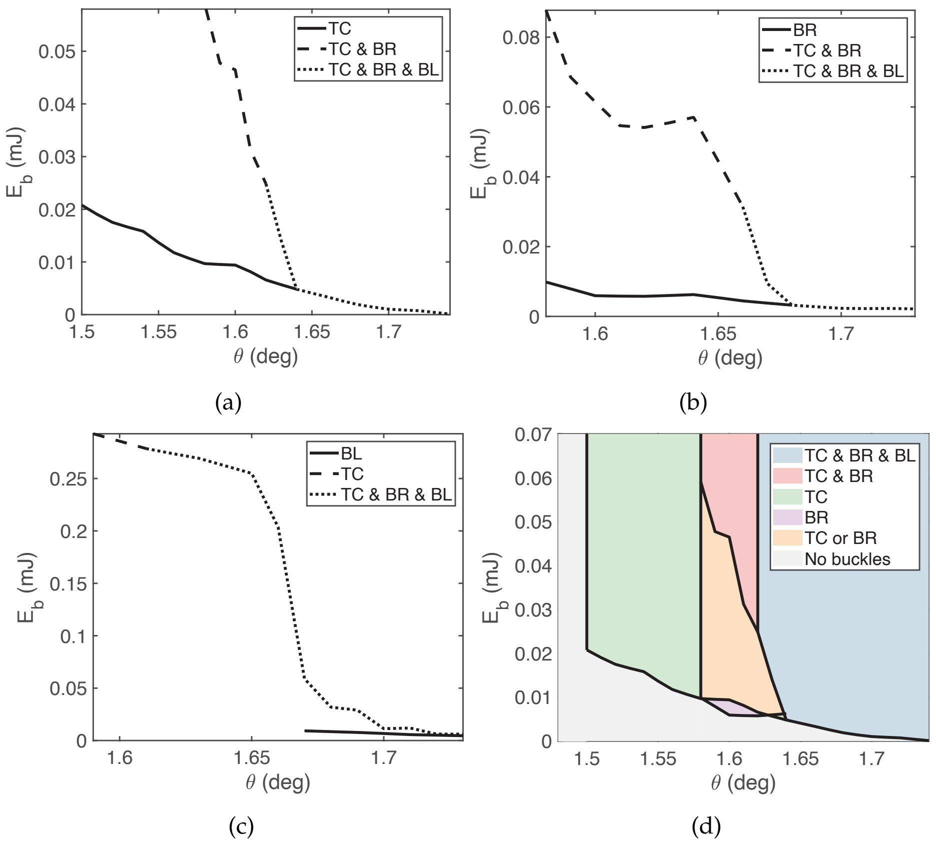

Figure 7: Energy barriers to form specific combinations of buckles before the bifurcation point, for (a) TC , (b) BR, and (c) BL probing. (d) Transition diagram that combines plots (a-c).

load and ends at the bifurcation point, corresponding to the formation of the single BL buckle. Contrary to the TC and BL probing, no full buckling pattern snaking is observed on this energy barrier branch. As previously observed, the energy barrier does not fall to 0 mJ at the bifurcation point, and the single BL buckle is broken away from the unbuckled state. The high energy barrier branch starting at $\theta = 1.49$ deg forms the single TC buckle, which evolves to the full buckling pattern at the three buckles minimal buckling rotation, $\theta = 1.61$ deg. Note that, as mentioned before, this specific rotation is in theory identical for the three probing schemes, and here agrees well with the three buckles minimum buckling rotation found for the TC probing location.

The energy barriers for the three probing locations have been combined Figure 7d to create a transition diagram that defines several regions in the (E_b-θ) plane. The boundaries are given by the minimum energy barrier required to achieve critical buckle configurations. For a given rotation and energy barrier level, the critical buckle configuration corresponds to the largest set of buckles that can remain in equilibrium. For instance, for $\theta = 1.7$ deg, the single BL buckle has a higher energy barrier than the TC and BR and BL buckle configuration. Since the single BL buckle also belongs to this larger set found at a lower energy barrier, it is not a critical configuration. In this representation, the probing location is removed and hence the energy barrier should be interpreted as a lower bound on the energy required for any perturbation to trigger buckling, regardless of where it is applied on the structure.

Above the single TC minimal buckling rotation ($\theta = 1.5$ deg), and below the TC snaking rotation ($\theta = 1.64$ deg), single buckle configurations (TC or BR) correspond to the lowest energy barriers. Above the TC snaking rotation, the three buckle configuration (TC and BR and BL) is the easiest to trigger.

5. Probing alternate post-buckling modes

(a) Search for critical buckling locations

The previous section has focused on studying the main post-buckling mode. The probing locations were determined after performing an initial buckling test, in which the location of the local peak displacement had been identified. Obviously, this approach requires the structure to buckle in order to determine the probing locations, which it is not an issue for the present structure, since the post-buckling regime is stable and the structure remains in its elastic domain after buckling. However, for other types of structure, such as cylindrical shells, buckling is likely to damage the structures and cause them to permanently deform. Therefore, several studies have attempted to determine the locations of localized buckling deformations, through specific probing methodologies and without triggering any buckling.

Recent work on cylindrical shells has shown that probing can be used to track the stability landscape's ridge and, by extrapolation, find the bifurcation point [42] without ever buckling the structure. It has also been envisioned that a similar approach can be used to trace the valley of the stability landscape and, by extrapolation, the minimum buckling load can be determined [22].

A common challenge is determining the location at which the localized buckling will first appear. In recent experiments, a defect was introduced in a soda can to pin the location of buckling [42] and therefore uniquely identify the location of probing. Even if the introduced imperfection was small, weakening the structure in this way may not be acceptable for engineering components such as rocket fuel tanks [7]. Recent analysis has shown that probing away from the dominant imperfection can lead to inaccurate buckling load predictions [43,44].

The approach adopted in the present study is different, as probing at different locations was carried out, without assuming any prior knowledge of the expected post-buckling shape. A characteristic of the specific structure under study, which simplifies this approach, is that the maximum compressive stresses in the structure occur along the edges of the longerons, and hence only a one-dimensional spatial scan of a longeron edge is required.

(b) Probing along longeron's edge and broken-away modes

Probing of the bottom longeron was carried out under fixed rotations of the structure, ranging from $\theta = 1.5$ deg to $\theta = 1.7$ deg. Note that these values are below the rotation that causes spontaneous buckling of the structure. 17 equally spaced locations, along the edge of the longeron under compression and starting and ending half-way between the acrylic plates and the end battens (the size of the probing stage did not allow probing near the acrylic plates), were investigated. The maximum probe displacement was initially set to $U_{p-max} = 3$ mm but excessive motion of the vertical linear bearing was observed for probe locations over 625 mm and hence the displacement was reduced to 1.5 mm.

The distance between probe locations was 36 mm and the measured probe forces were interpolated between probe locations to construct the map of the probe force as a function of the probe displacement and location, shown in Figure 8b for $\theta = 1.65$ deg. The schematic of the strip in Figure 8a is aligned with Figure 8b such that the probe coordinate directly corresponds to its physical location on the strip. The maximum probe force has been capped at 0.45 N and all dark red regions in Figure 8b correspond to probe forces above this threshold.

A periodic pattern of alternating local probe force maxima and minima is observed, with the maxima corresponding to probe locations aligned with a batten. This observation indicates that there is only one buckle forming between two battens, at a location close to (or at) the midpoint.

Two features are of particular interest in plots of this type. First, a zero probe force minimum would indicate a buckle that can be sustained in equilibrium at a specific probe location, and for a specific value of the rotation. These minima are referred to as equilibrium points. As a reminder, Figure 8b has been obtained for $\theta = 1.65$ deg and there are no negative minima in this specific case since the probe would lose contact with the structure as soon as the force reaches zero. Second,

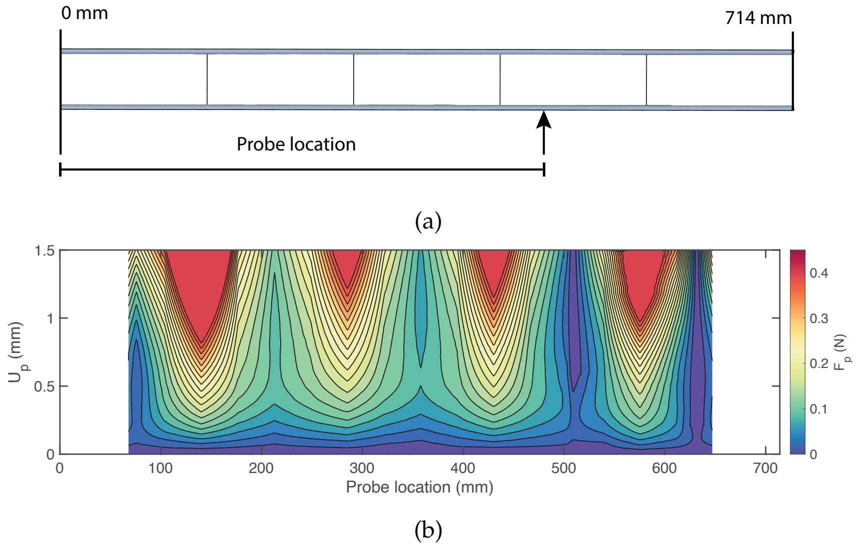

Figure 8: (a) Schematic of edge probing experiment and (b) map of probe force as a function of probe displacement and location, for $\theta = 1.65$ deg.

a positive local minimum (non-monotonic probe force profile) may indicate that a buckle could form at a probe location, but for higher values of the rotation. This situation can be encountered when the stability landscape valley is detected (see Figure 5 for instance) below the minimum buckled state. These positive local minima are referred to as valley points.

It is interesting to analyze the equilibrium points and valley points in Figure 8b. An equilibrium point is detected at location BR and a valley point is found at location BL. They correspond to the buckles already studied in the previous section, and stem from the TC buckle forming through a snaking sequence. Additional buckling locations are revealed. In particular, an equilibrium point is located at a probe location of 510 mm. This buckle does not appear in the main snaking sequence, and is therefore not connected to the fundamental path. It is a broken-away mode which can only be triggered if a disturbance is applied to the structure. An important observation is that the location of this mode corresponds to the buckles observed in Figure 4d, which was predicted by the FEM but so far not observed experimentally. At a probe location of 213 mm, the probe force profile features a valley point. However, probing for higher values of the rotation (the results for such cases are not included in the paper) indicates that this minimum is always positive for rotations below the spontaneous buckling. Finally, a last valley point is encountered at a probe location of 357 mm. It is also a broken-away mode and corresponds to the mirror symmetry of buckle TC for the bottom longeron. While in the simulation top and bottom longerons are interchangeable, gravity may ~~bias the experimental behavior of the structure towards the formation of TC rather than its bottom longeron counterpart.~~ introduce an additional compressive stress component on the top longeron, therefore biasing the experiment behavior towards the formation of TC rather than its bottom longeron counterpart.

Repeating the experiment on the top longeron yielded an almost identical contour map (not shown). Local buckling equilibria were found at the probe location TC (as expected from Section 4) and at 213 mm, similar to the alternate mode discussed above. Broken away modes were found for the left and right probe locations (counterpart of BL and BR on the top longeron) and belong to the snaking triggered by the bottom central buckle.

The spacing between probe locations used in the present study is rather coarse, although adequate for the specific structure. Other structures may require a finer discretization. Simulations could be harnessed to compute the probing region of influence and thus determine an appropriate spacing. Also, the density of probe locations in specific regions of interest could be increased as the test progresses.

(c) Triggering alternate buckling modes (BA and TA)

The previous experiment determined two alternate locations at which buckling can be triggered. One on the bottom longeron at a probe location of 510 mm, and another one on the top longeron at a probe location of 213 mm. These probe locations are called Bottom-edge Alternate (BA) and Top-edge Alternate (TA).

This section presents the results of probing conducted at these two locations, for $1.2 < \theta < 2$ deg. The initial rotation increment was 0.05 deg, refined to 0.02 deg for $\theta > 1.55$ deg. The corresponding stability landscapes are shown in Figure 9.

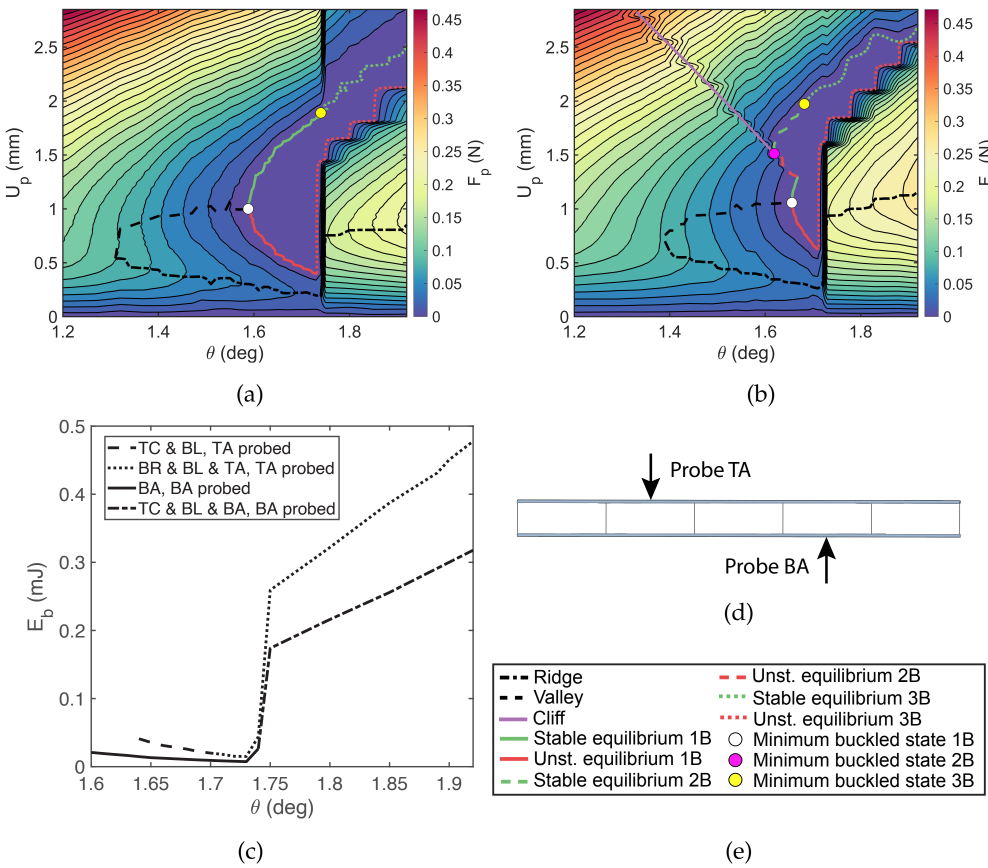

Figure 9: Stability landscapes for (a) BA, (b) TA probe locations and (c) energy barriers. (d) Schematic of strip structure showing probe locations. (e) Legend.

The BA probe location is discussed first. The stability landscape, shown in Figure 9a, is similar to the landscapes for the TC, BL, and BR probe locations for rotations below the point of spontaneous buckling. It features a ridge and a valley, both starting at $\theta = 1.31$ deg. The minimum buckling load to sustain the BA buckle is $\theta = 1.59$ deg. The minimally buckled state marks the start of the single-buckle stable and unstable equilibrium contours. At the structure's bifurcation point of $\theta = 1.74$ deg there is still a significant hill of probe force separating the unbuckled state and the unstable equilibrium contour. At this critical rotation, and in the absence of the BA buckle, the structure's main post-buckling mode forms, as previously seen in Figure 4e. For $\theta > 1.74$ deg, $U_p = 0$ mm corresponds to the end of the main post-buckling snaking sequence from the unbuckled state, as probing is applied to the buckled structure. For larger rotations the probing behavior changes significantly. The initial probe characteristic is steeper and the ridge is offset to $U_p = 0.8$ mm, with a large region of higher probe forces. When the probe displacement increases further, the structure experiences a snap-back and the unstable three buckles (BA, BL and TA) equilibria are found.

This new landscape topology can be explained as follows. Once the structure deforms into its main post-buckling mode, the formation of buckle BA requires buckle BR to disappear, which requires larger probe forces to be applied at the probe location. Notice that if the BA buckle is formed before the bifurcation point, the buckled equilibrium evolves to the three buckles (BA, BL and TA) configuration for $\theta > 1.74$ deg.

Next, the TA probe location is considered. The stability landscape for this case is shown in Figure 9b. The landscape features a ridge and a valley, both starting at $\theta = 1.39$ deg and a single buckle minimum buckling rotation of $\theta = 1.66$ deg. The TA buckle is also a broken away mode and at the bifurcation point the unstable equilibrium contour is farther away from the unbuckled state than it was for the BA buckle. This observation suggests that the TA buckle is harder to trigger.

For $\theta > 1.66$ deg the behavior is similar to that observed for the BA location. There is a large region of high magnitude probe forces between the unbuckled state and the unstable equilibrium contour, which physically corresponds to the probe force required for the TC buckle to disappear and the TA buckle to form. The TC buckle is the largest among the three buckles found in the main post-buckling mode and hence the amount of probe work needed to remove it is also largest.

The main difference between the BA and TA probe locations is the nature of the stable equilibria encountered while probing. Probing at the BA location leads to the formation of the BA buckle only, whereas probing at the TA location triggers the three buckle configuration. For $\theta < 1.62$ deg, the probe characteristic features a cliff, similar to the TC, BR, and BL landscapes (Section 4). When the cliff is reached, the structure experiences a snap-back caused by a fold (cusp catastrophe), and the bottom left buckle (BL) is triggered. However no equilibrium solution is found for the BL buckle when retracting the probe. Instead, the structure converges to the two buckles minimally buckled state for $\theta = 1.62$ deg. This state marks the start of the two buckles stable and unstable equilibrium contours on which the TC and BL buckles can coexist. The stable single buckle and unstable two buckles equilibrium contours meet at the snaking rotation of $\theta = 1.67$ deg. Finally, the two buckles equilibria evolve to the three buckles equilibria (TA, BR, and BL) for $\theta > 1.68$ deg.

Similarly to the analysis of Section 4, the probe force/displacement characteristic was integrated to compute the energy barrier for the various buckle configurations. The results are shown in Figure 9c. For both probing locations, the energy barrier features two regimes, before and after the formation of the main post-buckling mode. For $\theta < 1.74$ deg, the energy barrier is low ($E_b < 0.05$ mJ). For $\theta > 1.74$ deg, the energy barrier increases by almost an order of magnitude. As explained previously, this increase can be explained by the additional amount of energy that needs to be provided to the structure to make the BR and TC buckles disappear. Note that the energy barrier for the single TA buckle has not been reported in Figure 9 since it only corresponds to a very small range of rotations (0.01 deg).

It is concluded that probing at BA yields a lower energy barrier, over the entire range of rotations and therefore this is the critical alternate mode which is the most likely to appear if a perturbation is applied to the structure.

The present analysis has highlighted that it is possible to form alternate buckling modes, disconnected from the unbuckled state, and that switching between paths in the post-buckling regime is achievable but requires significantly more energy. The energy barriers for the TA and BA probe locations are compared to the energy barrier for the TC probe location, in Figure 10a. As a reminder, TC is the critical buckle for the main post-buckling mode, as it requires the least amount of energy to be formed. The energy required to form the BA buckle is about twice the energy required to form the TC buckle, and can only be formed for $\theta > 1.6$ deg, whereas the TC buckle can be formed for $\theta > 1.5$ deg.

Similarly to Section 4, the energy barriers in Figure 10a can be combined to obtain a transition diagram whose boundaries correspond to the critical buckle configurations, as shown in Figure

10b. This diagram identifies three regions: two with higher energy barriers that correspond to probing at the TA location, and the critical alternate mode BA with lower values of the energy barrier. This alternate transition diagram has been superimposed on the main post-buckling transition diagram (dotted lines) of Figure 7d. The resulting figure represents the competition between buckle configurations, characteristic of the structure's meta-stable state close to the spontaneous buckling rotation. Comparison of the energy barriers for the alternate modes and the main transition shows that a larger disturbance is required to reach the alternate modes.

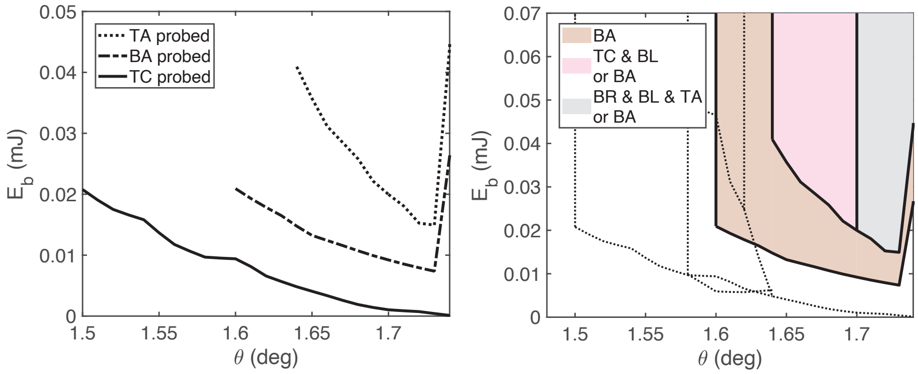

(a) (b)

Figure 10: (a) Energy barrier comparison between TC, BA, and TA probe locations and (b) transition diagram characterizing the formation of alternate buckling modes. The transition diagram for the main post-buckling mode is shown in dotted lines.

(d) Large rotation response

In Section 3 it was found that the strip's main post-buckling path is stable and that the structure is able to withstand bending moments larger than the spontaneous buckling moment. The maximum load-bearing capacity of the structure before failure is of interest, where failure is defined as the structure's stiffness decreasing to zero, which corresponds to a horizontal tangent in the moment/rotation characteristic.

Without any disturbance applied to the structure, the main post-buckling mode – consisting of local buckles at locations BR, BL, and TC— appears when the spontaneous buckling rotation is exceeded. The full main post-buckling response is shown as a solid line in Figure 11a. As the rotation is increased, the amplitude of the buckles gradually increases, until a global in-plane bending of the strip can be observed. The maximum moment is $M_{max} = 2.35$ Nm, for $\theta = 8.7$ deg. Beyond this critical rotation, the structure experiences a snap-back, which physically corresponds to a large increase in the TC buckle amplitude that makes the cross-section almost flat locally. The deformed shape is shown in Figure 11b. Note that this specific mode of failure has been observed previously for similar structures [31,32].

The previous subsection has demonstrated that the BA buckle can be in equilibrium on the structure. Next, a small perturbation was applied to the structure and probing was conducted at the BA probe location such that the critical alternate buckle would be formed right before reaching the spontaneous buckling rotation. The purpose of this test was to understand whether this specific buckle can be the start of an alternate snaking sequence, to the the TC buckle that triggered the main snaking sequence. In other words, can the competition between two local buckles, TC and BA, yield significant differences in the structure's global response?

Beyond the point of spontaneous buckling, additional buckles form simultaneously at locations BL and TA, and the buckle BA remains. Next, the rotation was increased to trace the entire post-buckling characteristic, and the results are shown as a dotted line in Figure 11a. The main and alternate post-buckling paths are practically identical until $\theta = 2.6$ deg. At this

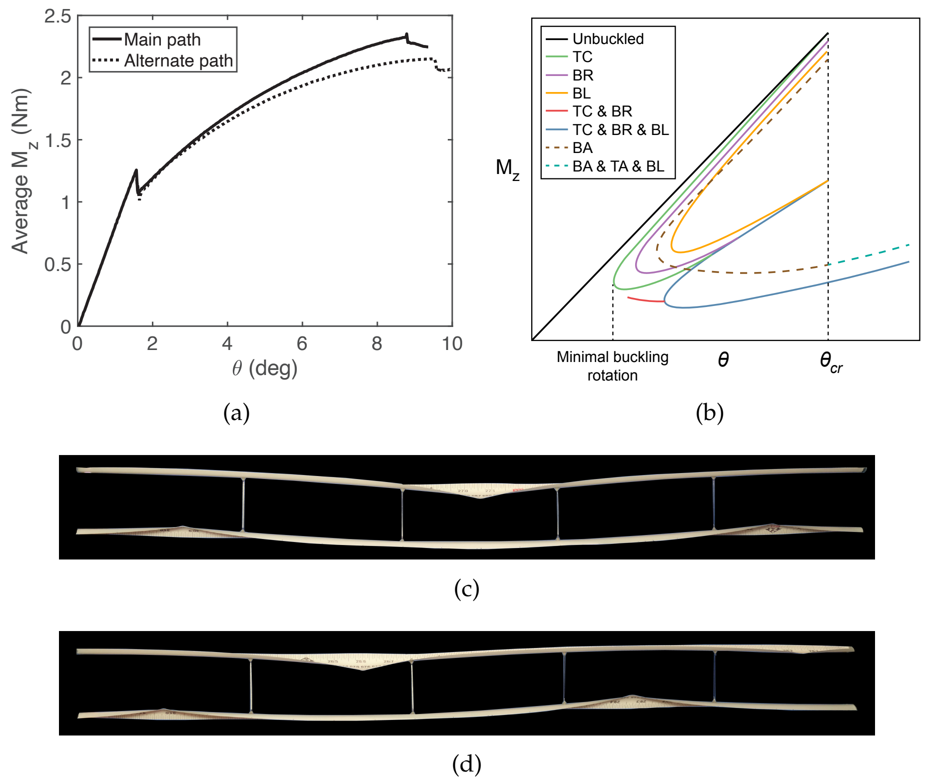

Figure 11: (a) Full post-buckling response obtained for the main (connected by bifurcation) post-buckling path, and the alternate (broken away) post-buckling path. (b) Schematic of paths leading to main and alternate post-buckling deformed shapes. (c) Main and (d) alternate post-buckling deformed shape.

rotation, an additional buckle forms on the top longeron, in the middle of the rightmost batten pair. After this rotation is exceeded, the main and alternate post-buckling responses diverge, with the alternate post-buckling path showing a decreased stiffness. It ultimately yields a lower value of the maximum moment, $M_{max} = 2.15$ Nm, for a higher value of rotation, $\theta = 9.5$ deg. The deformed shape obtained at the end of the alternate post-buckling path is shown in Figure 11d. At $\theta = 9.5$ deg, the structure experiences a snap-back corresponding to the sudden increase in the TA buckle's amplitude. Similarly to the deformed shape for the main post-buckling, the cross-section becomes locally flat also in this case. For the main deformed shape, the two alternating buckles are separated by double the batten spacing, whereas for the alternate deformed shape the spacing between the buckles is equal to a single batten spacing. This difference in spacing allows the structure to feature four buckles for the alternate snaking sequence whereas it only features three for the main sequence.

These experiments have highlighted two competing post-buckling sequences, stemming from the TC and BA buckles. Based on the stability landscapes and energy barriers in Sections 4 and 5, multiple post-buckling paths leading to these two sequences have been sketched in Figure 11b. With the current experimental setup, it would be possible to record the bending moment while probing, and therefore locate these paths exactly in the moment/rotation plane.

Globally, it has been shown that if a small amount of energy disturbs the structure and triggers the BA buckle, the maximum moment decreases by 9% and the bending stiffness above $\theta = 1.6$ deg is decreased. The deformed shapes of the structure are also different. While both characteristics are stable and the difference in behavior can be seen as minor, it will not necessarily be the case in all structures. Generally, a competition between local buckles can potentially cause significant differences in post-buckling response and stability.

6. Conclusion

Bending experiments were conducted on a thin-shell structure consisting of two open cross-section longerons connected by transverse battens. Similar structures are being developed for use in large deployable spacecraft [45,46]. An important characteristic of these structures is that they feature a stable post-buckling regime under bending, and therefore they can carry loads significantly larger than their initial buckling load. This characteristic opens new design possibilities in which structures are designed to reach close to their initial buckling load, and possibly even enter the post-buckling regime. Through this approach, the mass efficiency could be greatly improved by adopting lower than standard safety factors.

This paper has used experimental probing to characterize the structure's meta-stability close to the buckling load. By locally displacing the longeron's edge under compression while recording the probe force for various values of the imposed end rotation, stability landscapes were constructed and the stability of local buckles forming in the structure was characterized. Of particular interest was the minimum rotation at which buckles can appear in the structure, and the level of disturbance that can lead to buckle formation prematurely.

A transition diagram, derived from the experiments, has defined regions in the (E_b-θ) plane for which specific combinations of buckles can appear. If buckling is to be avoided, the transition diagram can serve as a tool to derive tight lower bounds on the allowable end rotation, allowing buckling criteria tailored to specific perturbations and imperfections present in the real environment. For instance, in an environment where perturbations are limited and quantifiable, one can set a bound on the minimum allowable energy barrier and use the transition diagram to find the corresponding value of the maximum allowable rotation. The diagram also allows relaxed buckling criteria to be adopted if a limited number of buckles is allowed to form during operation. However, in an environment where perturbations are hard to quantify, one could use the minimum buckling rotation as a conservative buckling criterion.

Probing applied along the length of the longerons has led to the detection of two broken-away modes. These modes are disconnected from the structure's fundamental path, although they are accessible through a disturbance applied to the structure. These modes directly compete with the main post-buckling mode. For the specific structure presented in this paper, the energy barrier to trigger the alternate modes is about twice that required for the main critical buckle. However, tests on other structures has shown that the two energy barriers can be almost identical, and hence these alternate modes cannot be neglected.

Probing these alternate modes yielded an alternate transition diagram that was superimposed on the main buckling transition diagram to obtain a complete picture of the structure's meta-stability close to buckling. The analysis also showed that the alternate buckles can also be triggered after the main post-buckling mode has appeared, although this transition requires a greater amount of energy to be provided.

Finally, large rotation experiments were performed and it was found that the formation of the critical alternate buckle triggers a full snaking sequence featuring four buckles, as opposed to three buckles in the main post-buckling snaking sequence. These two competing responses yielded different maximum moments at the point of failure.

This study has highlighted the importance of characterizing the structure's response for all possible buckling modes, if a structure is to be used in its post-buckling regime. It has been emphasized that in order to design and operate thin-shell structures near their buckling point, or even in their post-buckling regime, finite element simulations are helpful but not sufficient to characterize all of the possible responses. The finite element analysis of Section 2 did in fact predict the two competing post-buckling shapes observed in the experiments. However, while the lowest bifurcation and therefore the connected path was in theory obtained for the first eigenmode imperfection, the solution obtained for the second eigenmode imperfection was in fact observed only in the experiments. Intrinsic imperfections in the real geometry biased the structure to follow mainly its second eigenmode.

According to the framework developed in this paper, an engineer would consider the whole set of theoretical post-buckling solutions and for each one focus on characterizing its stability and the energy needed to trigger it. This approach paves the way to highly optimized buckling criteria tailored to specific applications.

Lastly, it should be noted that imperfection-insensitive structures have been proposed as an approach to reducing buckling uncertainty. Exemplar designs have been developed for particular structures, such as cylindrical and spherical shells [47,48]. The probing methodology of the present paper could serve as an efficient tool to design imperfection insensitive structures.

Acknowledgments

Financial support from the Space Solar Power Project at Caltech is gratefully acknowledged.

References

1. J. Banik, S. Kiefer, M. LaPointe, P. LaCorte, On-orbit validation of the Roll-Out Solar Array, 2018 IEEE Aerospace Conference (2018). doi:10.1109/AERO.2018.8396390.
2. J. M. Fernandez, G. Rose, O. R. Stohlman, C. J. Younger, G. D. Dean, J. E. Warren, J. H. Kang, R. G. Bryant, K. W. Wilkie, An advanced composites-based solar sail system for interplanetary small satellite missions, AIAA Spacecraft Structures Conference, AIAA 2018-1437 (2018). doi:10.2514/6.2018-1437.
3. T. Von Karman, H.-S. Tsien, The buckling of thin cylindrical shells under axial compression, Journal of the Aeronautical Sciences 8 (8), 303–312 (1941). doi:10.2514/8.10722.
4. L. H. Donnell, C. C. Wan, Effect of imperfections on buckling of thin cylinders and columns under axial compression, Journal of Applied Mechanics 17 (1), 73–83 (1950).
5. W. T. Koiter, On the Stability of Elastic Equilibrium., H. J. Paris, Amsterdam, 1945, Ch. 8, pp. 201–213.
6. NASA, Buckling of thin-walled circular cylinders. NASA Space Vehicle Design Criteria, NASA SP-8007 (revised 1968), NASA (1965).
7. M. Hilburger, Developing the next generation shell buckling design factors and technologies, 53rd AIAA/ASME/ASCE/AHS/ASC Structures, Structural Dynamics and Materials Conference, AIAA 2012-1686 (2012). doi:10.2514/6.2012-1686.
8. A. Lee, F. López Jiménez, J. Marthelot, J. W. Hutchinson, P. M. Reis, The geometric role of precisely engineered imperfections on the critical buckling load of spherical elastic shells, Journal of Applied Mechanics 83 (11): 111005 (2016). doi:10.1115/1.4034431.
9. G. Tzortzinis, C. Ai, S. F. Breña, S. Gerasimidis, Using 3D laser scanning for estimating the capacity of corroded steel bridge girders: Experiments, computations and analytical solutions, Engineering Structures, 265; 114407 (2022). doi.org/10.1016/j.engstruct.2022.114407.
10. M. K. Wadee, G. W. Hunt, A. I. M. Whiting, Asymptotic and Rayleigh-Ritz routes to localized buckling solutions in an elastic instability problem, Proceedings of the Royal Society of London. Series A: Mathematical, Physical and Engineering Sciences 453 (1965) 2085–2107 (1997). doi:10.1098/rspa.1997.0112.
11. J. W. Hutchinson, Buckling of spherical shells revisited, Proceedings of the Royal Society A: Mathematical, Physical and Engineering Sciences 472 (2195): 20160577 (2016) . doi:10.1098/rspa.2016.0577.
12. B. Audoly, J. W. Hutchinson, Localization in spherical shell buckling, Journal of the Mechanics and Physics of Solids 136, March, 103720 (2020). doi:https://doi.org/10.1016/j.jmps.2019.103720.
13. J. W. Hutchinson, J. M. T. Thompson, Nonlinear buckling behaviour of spherical shells: barriers and symmetry-breaking dimples, Philosophical Transactions of the Royal Society A: Mathematical, Physical and Engineering Sciences 375 (2093) 20160154 (2017). doi:10.1098/rsta.2016.0154.
14. G. Hunt, G. Lord, A. Champneys, Homoclinic and heteroclinic orbits underlying the post-buckling of axially-compressed cylindrical shells, Computer Methods in Applied Mechanics and Engineering 170 (3), 239–251 (1999). doi:https://doi.org/10.1016/S0045-7825(98)00197-2.

15. R. M. J. Groh, A. Pirrera, On the role of localizations in buckling of axially compressed cylinders, Proceedings of the Royal Society A: Mathematical, Physical and Engineering Sciences 475 (2224), 20190006 (2019). doi:10.1098/rspa.2019.0006.
16. T. Kreilos, T. M. Schneider, Fully localized post-buckling states of cylindrical shells under axial compression, Proceedings of the Royal Society A: Mathematical, Physical and Engineering Sciences 473 (2205), 20170177 (2017). doi:10.1098/rspa.2017.0177.
17. J. Horák, G. J. Lord, M. A. Peletier, Cylinder buckling: The mountain pass as an organizing center, SIAM Journal on Applied Mathematics 66 (5), 1793–1824 (2006). doi:10.1137/050635778.
18. J. M. T. Thompson, L. N. Virgin, Spatial chaos and localization phenomena in nonlinear elasticity, Physics Letters A 126 (8), 491 – 496 (1988). doi:https://doi.org/10.1016/0375-9601(88)90045-X.
19. J. M. T. Thompson, Advances in shell buckling: Theory and experiments, International Journal of Bifurcation and Chaos 25 (01), 1530001 (2015). doi:10.1142/S0218127415300013.
20. J. M. T. Thompson, J. Sieber, Shock-sensitivity in shell-like structures: with simulations of spherical shell buckling, International Journal of Bifurcation and Chaos 26 (02), 1630003 (2016). doi:10.1142/S0218127416300032.
21. J. W. Hutchinson, J. M. T. Thompson, Nonlinear buckling interaction for spherical shells subject to pressure and probing forces, Journal of Applied Mechanics 84 (6), 061001 (2017). doi:10.1115/1.4036355.
22. E. Virot, T. Kreilos, T. M. Schneider, S. M. Rubinstein, Stability landscape of shell buckling, Phys. Rev. Lett. 119, 224101 (2017). doi:10.1103/PhysRevLett.119.224101.
23. J. Marthelot, F. López Jiménez, A. Lee, J. W. Hutchinson, P. M. Reis, Buckling of a pressurized hemispherical shell subjected to a probing force, Journal of Applied Mechanics 84 (12), 121005 (2017). doi:10.1115/1.4038063.
24. J. M. T. Thompson, G. H. M. van der Heijden, Quantified "shock-sensitivity" above the Maxwell load, International Journal of Bifurcation and Chaos 24 (03), 1430009 (2014). doi:10.1142/S0218127414300092.
25. S. Gerasimidis, E. Virot, J. W. Hutchinson, S. M. Rubinstein, On establishing buckling knockdowns for imperfection-sensitive shell structures, Journal of Applied Mechanics 85 (9), 091010 (2018). doi:10.1115/1.4040455.
26. J. Shen, R. Groh, M. Schenk, A. Pirrera, Experimental path-following of equilibria using newton's method. Part i: Theory, modelling, experiments, International Journal of Solids and Structures 210-211, 203–223 (2021). doi:https://doi.org/10.1016/j.ijsolstr.2020.11.037.
27. J. Shen, R. Groh, M. Schenk, A. Pirrera, Experimental path-following of equilibria using newton's method. part ii: Applications and outlook, International Journal of Solids and Structures 213, 25–40 (2021). doi:https://doi.org/10.1016/j.ijsolstr.2020.11.038.
28. J. Shen, R. M. Groh, M. A. Wadee, M. Schenk, A. Pirrera, Probing the stability landscape of prestressed stayed columns susceptible to mode interaction, Engineering Structures 251, 113465 (2022). doi:https://doi.org/10.1016/j.engstruct.2021.113465.
29. M. Arya, N. Lee, S. Pellegrino, Ultralight structures for space solar power satellites, 3rd AIAA Spacecraft Structures Conference, AIAA 2016-1950 (2016). doi:10.2514/6.2016-1950.
30. F. Royer, S. Pellegrino, Ultralight ladder-type coilable space structures, AIAA Scitech Forum, AIAA 2018-1200 (2018). doi:10.2514/6.2018-1200.
31. F. Royer, S. Pellegrino, Buckling of ultralight ladder-type coilable space structures, AIAA Scitech Forum, AIAA 2020-1437 (2020). doi:10.2514/6.2020-1437.
32. F. Royer, S. Pellegrino, Probing the stability of ladder-type coilable space structures, AIAA Journal 60 (4), 2000–2012 (2022). doi:10.2514/1.J060820.
33. F. Royer, J. W. Hutchinson, S. Pellegrino, Probing the stability of thin-shell space structures under bending, International Journal of Solids and Structures (2022). doi:10.1016/j.ijsolstr.2022.111806.
34. K. Miura, S. Pellegrino, Forms and Concepts for Lightweight Structures, Cambridge University Press, Cambridge (2020). doi.org/10.1017/9781139048569.
35. F. Royer, Probing the buckling of thin-shell space structures, Ph.D. thesis, California Institute of Technology (2021). doi:10.7907/ksn2-t598.
36. C. Leclerc, S. Pellegrino, Nonlinear elastic buckling of ultra-thin coilable booms, International

Journal of Solids and Structures 203 (10), 46–56 (2020). doi:https://doi.org/10.1016/j.ijsolstr.2020.06.042.

37. E. Riks, An incremental approach to the solution of snapping and buckling problems, International Journal of Solids and Structures 15 (7), 529–551 (1979). doi:10.1016/0020-7683(79)90081-7.

38. T. Rahman, E. Jansen, Finite element based coupled mode initial post-buckling analysis of a composite cylindrical shell, Thin-Walled Structures 48 (1), 25 – 32 (2010). doi:https://doi.org/10.1016/j.tws.2009.08.003.

39. R. M. J. Groh, A. Pirrera, Spatial chaos as a governing factor for imperfection sensitivity in shell buckling, Physical Review E, 100, 032205 (2019). doi:10.1103/PhysRevE.100.032205.

40. R. Groh, D. Avitabile, A. Pirrera, Generalised path-following for well-behaved nonlinear structures, Computer Methods in Applied Mechanics and Engineering 331, 394 – 426 (2018). doi:https://doi.org/10.1016/j.cma.2017.12.001.

41. G. Hunt, E. Lucena Neto, Localized buckling in long axially-loaded cylindrical shells, Journal of the Mechanics and Physics of Solids 39 (7), 881 – 894 (1991). doi:https://doi.org/10.1016/0022-5096(91)90010-L.

42. A. Abramian, E. Virot, E. Lozano, S. M. Rubinstein, T. M. Schneider, Nondestructive prediction of the buckling load of imperfect shells, Physical Review Letters 125, 225504 (2020). doi:10.1103/PhysRevLett.125.225504.

43. K. K. Yadav, N. L. Cuccia, E. Virot, S. M. Rubinstein, S. Gerasimidis, A nondestructive technique for the evaluation of thin cylindrical shells' axial buckling capacity, Journal of Applied Mechanics 88 (5), 051003 (2021). doi:10.1115/1.4049806.

44. A. Abbasi, D. Yan, P. M. Reis, Probing the buckling of pressurized spherical shells, Journal of the Mechanics and Physics of Solids 155, 104545 (2021). doi:https://doi.org/10.1016/j.jmps.2021.104545.

45. E. Gdoutos, C. Leclerc, F. Royer, D. A. Türk, S. Pellegrino, Ultralight spacecraft structure prototype, AIAA Scitech Forum, AIAA 2019-1749 (2019). doi:10.2514/6.2019-1749.

46. E. Gdoutos, A. Truong, A. Pedivellano, F. Royer, S. Pellegrino, Ultralight deployable space structure prototype, AIAA Scitech Forum, AIAA 2020-0692 (2020). doi:10.2514/6.2020-0692.

47. X. Ning, S. Pellegrino, Imperfection-insensitive axially loaded thin cylindrical shells, International Journal of Solids and Structures 62 (6), 39 – 51 (2015). doi:https://doi.org/10.1016/j.ijsolstr.2014.12.030.

48. X. Ning, S. Pellegrino, Searching for imperfection insensitive externally pressurized near-spherical thin shells, Journal of the Mechanics and Physics of Solids 120 (11), 49 – 67 (2018). doi:https://doi.org/10.1016/j.jmps.2018.06.008.